

A New *in-situ* Exsolution Supporting Framework for Metal Nanoparticle Growth

Mengchu Wang

Zhejiang University

Bike Zhang

Zhejiang University

Jiaqi Ding

Zhejiang University

Fanxing Zhang

Zhejiang University

Rui Tu

Zhejiang University

Matthew Bernards

University of Idaho <https://orcid.org/0000-0002-5234-1910>

Yi He (✉ yihezj@zju.edu.cn)

Zhejiang University <https://orcid.org/0000-0002-8807-0892>

Pengfei Xie

Zhejiang University <https://orcid.org/0000-0002-7644-9934>

Yao Shi

Zhejiang University

Article

Keywords: catalysis, in-situ exsolved metal nanoparticles, electrocatalysis

Posted Date: July 30th, 2021

DOI: <https://doi.org/10.21203/rs.3.rs-750543/v1>

License:   This work is licensed under a Creative Commons Attribution 4.0 International License.

[Read Full License](#)

Abstract

Catalysts made of *in-situ* exsolved metal nanoparticles often demonstrate promising activity and high stability in many applications. However, the design of these catalysts is greatly constrained by the classic exsolution mechanism, which occurs almost exclusively through substitutional metal-doping in perovskites. Here we show that metal nanoparticles can also be *in-situ* exsolved from interstitially doped metal cations in a NiOOH supporting framework with the guidance of theoretical calculation. The exsolution can be conducted swiftly at room temperature. A novel copper nanocatalyst prepared with this approach have a *quasi*-uniform size of 4 nm delivering an exceptional CO faradaic efficiency of 95.6% with a notable durability for the electrochemical reduction of CO₂. This design principle is further proven to be generally applicable to other metals and foregrounded for guiding the development of advanced catalytic materials.

Main Text

Catalysts based on supported metal nanoparticles (NPs) are broadly used in energy conversion and storage processes.^{1,2} The *in situ* exsolution with perovskites emerges as time-saving and cost-effective way to fabricate NPs catalysts,³⁻⁶ because of that this approach does not need multiple deposition steps or expensive precursors, while producing better-distributed and agglomeration-resistant metal NPs.⁷⁻¹⁰ However, the exsolution of NPs from perovskites (ABO₃) still faces several challenges. First of all, this process works with limited elements, as only the A/B sites with similar size can accommodate the formation of perovskite-type structure through a substitution mechanism. In addition, it is difficult to precisely control the composition of exsolved metal NPs due to the possibility of exsolution of both doping and doped metals.¹¹ Moreover, the exsolution approach poses high energy consumption as it is typically conducted at high temperatures of 700-1200 °C in a H₂ atmosphere.^{12,13} High temperature may also cause uncontrolled growth and coarsening of the NPs. Lastly, the growth of NPs takes a relatively long time (10–30 hours) due to sluggish kinetics.^{14,15} These drawbacks largely originate from the perovskite supporting framework. Therefore, in order to tackle these challenges, a new *in situ* exsolution supporting framework is needed.

Copper (Cu) has been well studied as the electrocatalysts for electrochemical reduction of CO₂ (ERCO₂).^{16,17} In particular, Cu NPs with smaller diameters (<6 nm) can prevent the hydrogenation of CO and favors the formation of synthetic gas (CO and H₂).¹⁸ However, the Cu NPs catalysts prepared in the wet-chemical impregnation or even traditional exsolution are generally not stable for longer operation due to susceptible agglomeration.¹⁹

Herein, we reported a new *in situ* exsolution of Cu NPs from nickel-based hydroxide (γ -NiOOH) with Cu cations confined in layer structures, denoted as Cu_xNiOOH, where x represents molar ratio of Cu to Ni (Figure 1A). *Ab initio* constrained molecular dynamics calculations demonstrate that the γ -NiOOH framework offers spontaneous *in situ* exsolution of Cu NPs from interstitial doped Cu, as evidenced by a

negligible exsolution free energy barrier (~ 0.07 eV, Figure 1B). In comparison, a much higher free energy barrier of Cu exsolution from a typical LaSrFeO_4 perovskite²⁰ is found to be 4.54 eV, necessitating a high temperature for this process (Figure 1C). This result intrinsically underlines the advantage of exsolution of Cu_xNiOOH at mild condition, which is further corroborated by a comprehensive comparison with other perovskites in term of exsolution temperatures (Figure 1D).²⁰⁻²⁷

With the guidance of molecular simulation, we synthesized Cu_xNiOOH , then applied the electrical activation, the obtained samples are denoted as $\text{Cu}_x@\text{NiOOH}$ (Figure S1). The framework was proven to be predominantly $\gamma\text{-NiOOH}$ with an intensive characteristic peak at 12.8° accompanied by tiny amount of $\beta\text{-Ni(OH)}_2$ and $\text{Ni(OH)}_2 \cdot 0.75\text{H}_2\text{O}$ in X-ray diffraction (XRD) patterns (Figure 2A). With the addition of copper, the peaks at 12.8° become sharpened and shift to lower angles, and no copper related peaks are observed when $\text{Cu/Ni ratio} \leq 1/2$, which is due to an expansion of $\gamma\text{-NiOOH}$ crystalline lattice with the doping of coppers.²⁸ While at $\text{Cu/Ni ratio} \geq 1/2$, the peaks corresponding to $\text{Cu(OH)}_2 \cdot 2\text{H}_2\text{O}$ appear. This suggests that the 1:2 Cu/Ni ratio is the upper limit of Cu doping, beyond which copper will exist as Cu(OH)_2 outside of the $\gamma\text{-NiOOH}$ framework.

The doping process observed above is also supported by the X-ray photoelectron spectroscopy (XPS) results (Figure S2), which demonstrate the existence of Ni(II) and Ni(III) featured as the binding energies of the Ni $2p_{3/2}$ spectra fall at 855.3 to 856.5 eV for $\gamma\text{-NiOOH}$,^{29,30} whereas the Ni $2p_{3/2}$ spectra for Cu-doped $\gamma\text{-NiOOH}$ shift to a higher energy value caused by the interactions of copper-nickel d-d band.³¹ And the peak areas for the Cu(OH)_2 species get higher with the increasing Cu doping level (Figure S3).

Moreover, Raman spectroscopy shows the existence of a wide peak located at $520\sim 550\text{ cm}^{-1}$ (Figure 2B). This is the E_g Ni-O bending vibration and A_{1g} Ni-O stretching vibration for $\gamma\text{-NiOOH}$.³² Compared to pristine $\gamma\text{-NiOOH}$, copper doped samples have peaks slightly shifted towards higher wavenumber, which can be attributed to lattice distortion caused by the doping of copper ions into the $\gamma\text{-NiOOH}$ structure.³³

X-ray absorption fine structure (XAFS) analysis shows that Cu was doped into the layered crystal structure of the $\gamma\text{-NiOOH}$ with an interstitial mechanism instead of the substitution mechanism observed with perovskites. Extended XAFS (EXAFS) fitting data reveals that the bond distances for Cu-O and Cu-Ni (Cu) are 1.95 \AA and 3.14 \AA (Figure S4, Table S1), respectively, which are larger than the distances for Ni-O (1.81 \AA) and Ni-Ni (2.82 \AA) in $\gamma\text{-NiOOH}$, ruling out the possibility of copper replacing Ni sites or embedding in any layer, instead copper is doped into the interstitial space of the $\gamma\text{-NiOOH}$ lattice. X-ray absorption near-edge structure (XANES) spectra further show that the doped Cu is in a +2 oxidation state as evidenced by the pre-edge intensity at $8970\sim 8980\text{ eV}$ (Figure 2C). Further, no subnanometer Cu or CuO microcrystalline was observed because the absence of Cu-Cu scatterings (Figure S5).

The exsolution process of Cu from $\text{Cu}_{0.5}\text{NiOOH}$ results are monitored by TEM and Raman after the electrochemical activation. TEM shows dark dots are formed on the surface of $\text{Cu}_{0.5}@\text{NiOOH}$, which are not present on $\text{Cu}_{0.5}\text{NiOOH}$ (Figure 2D). These dots represent the interlayer spacings of 0.181, 0.198,

0.213, 0.203, and 0.273 nm, corresponding to the (1 1 0), (-1 1 1), and (1 1 1) planes of CuO, the (1 1 1) plane of Cu₂O, and the (2 0 0) plane of metallic Cu, respectively (Figure S6). We calculate the distribution of particle sizes based on Figure 2D, and the average size of exsolved Cu was ~4 nm (Figure S7A). Raman (Figure 2E) also confirms the existence of CuO (280, 321 cm⁻¹) and Cu₂O (623 cm⁻¹) in Cu_{0.5}@NiOOH, which are absent in Cu_{0.5}NiOOH.

To understand the exsolution at atomic level, we calculate the structure of γ -NiOOH with one doped or exsolved Cu as shown in Figure 2F. Initially, the Cu cation is confined in NiOOH layers, coordinating with four O atoms, with an average bond length of 1.94 Å as that of the typical copper oxides.³⁴ With the cleavage of Cu-O mediated by electro-activation, Cu diffuses along the interlayers until stabilizing at the NiOOH (1 0 2) surface via a more weak Cu-O bonds with distance of ~ 2.10 Å. Figure 2G and Figure S8 further investigate the agglomeration with more Cu exsolved from bulk. It is interesting to find that less segregation energy is observed with the assembly of Cu, implying that a smaller size of copper would be expected which are consistent with TEM results. A Bader charge analysis determines the oxidation state of exsolved Cu close to zero with more Cu exsolved (Figure S9). Alternatively, under the working circumstances of negative potential (-0.3~-1.5 V vs. RHE), Cu cations are easy to be reduced to metallic state as reported by other literature.³⁵ It is noted that metallic Cu in Cu_x@NiOOH are easily oxidized when unavoidable exposure to air. Considering that Cu_{0.5}NiOOH are calcined in air but without copper oxides observed, the CuO and Cu₂O on Cu_{0.5}@NiOOH are likely formed by the oxidation of metallic Cu exsolved.

This new exsolution method offers several major advantages over the conventional perovskite-based framework (Figure 1D). Our exsolution can be achieved in as little as ~20 minutes through electrochemical activation at room temperature due to much lower barrier of 0.07 eV. In comparison, the exsolution with perovskites typically takes 10-30 hours due to the much higher energy of 4.54 eV. Moreover, our approach produces smaller Cu NPs (~4 nm) (Figure S7A) than a typical perovskite-based approach (10—2000 nm).²⁰⁻²⁷ As predicted by DFT results, the well-control of Cu NPs size is determined by segregation energy, which declines with more Cu exsolved, indicating that the formation of smaller Cu NPs is energy-favorable.

The exsolved Cu NPs from the γ -NiOOH exhibit high catalytic activity for ERCO₂ to CO (Table S2), which showing a volcano dependence on the size of exsolved Cu NPs resulting from different loading of doped Cu (Figure 3A, Figure S7B and S10), while the γ -NiOOH is also confirmed to be no activity, as no CO was observed (Figures 3C, S11 and S12), proving that exsolved Cu NPs are active sites.

Among all the tested catalysts, Cu_{0.5}@NiOOH with ~3.5 nm Cu NPs shows the highest activity for ERCO₂ (Figure 3A-3C), which can be explained by the availability of ultrafine Cu NPs exsolved from the framework. Specifically, at an applied potential of -0.7 V vs. RHE, the faradaic efficiency for CO (FE-CO) reached an unprecedented 95.6% with an acceptable CO current density (J_{CO}) of 10.6 mA cm⁻². In addition, The FE towards CO remains greater than 80% (Figure 3B) over a potential range between -0.5 V and -0.9 V.

To gain insight into the ER CO_2 performance of $\text{Cu}_{0.5}\text{@NiOOH}$, we investigated the electrochemical active surface area (ECSA). Larger ECSA indicates more active sites are available for the adsorption of reactants, thus facilitating CO evolution in ER CO_2 . The ECSA of $\text{Cu}_{0.5}\text{@NiOOH}$ (133.53 cm^2) is 1.38, 1.22, 1.03, and 1.61 times larger than that of $\text{Cu}_1\text{@NiOOH}$ (96.69 cm^2), $\text{Cu}_{0.7}\text{@NiOOH}$ (109.25 cm^2), $\text{Cu}_{0.3}\text{@NiOOH}$ (129.70 cm^2), and NiOOH (82.86 cm^2), respectively (Figure S13 and Table S3). These results further suggest that exsolved Cu NPs expose a large number of active sites. CO_2 adsorption measurements for $\text{Cu}_{0.5}\text{@NiOOH}$ exhibited an excellent CO_2 adsorption capacity of 99.8 mg g^{-1} , which facilitates ER CO_2 (Figure S14).

Electrochemical impedance spectroscopy (EIS) analysis of $\text{Cu}_{0.5}\text{@NiOOH}$ demonstrates the extremely low charge transfer resistance (R_{ct}) at the interface of the dip-coated catalyst and electrolyte (Figure 3D). Furthermore, the kinetics of the CO evolution was evaluated by tafel analysis. The tafel slop of $\text{Cu}_{0.5}\text{@NiOOH}$ was measured to be 103 mV dec^{-1} (Figure 3E), suggesting fast kinetics for the CO formation, which is close to the theoretical value (118 mV dec^{-1}), indicating that the one electron transfer is the rate-determining step (RDS) for the generation of CO.

The exsolved Cu NPs demonstrate a notable electrochemical stability. Both the current density and the corresponding FE-CO are stable during a 40 h electrolysis process (Figure 3F). Additionally, TEM and Raman show that the microstructure of NiOOH and exsolved Cu NPs are maintained (Figure 2E and S15).

To demonstrate general applicability of *in situ* exsolution from metal doped γ -NiOOH, we further examined the case of Mn and Zn. Raman shows three bands centered at 467 , 571 and 624 cm^{-1} in $\text{Mn}_{0.25}\text{@NiOOH}$ correspond to the MnO_2 , which are not present on $\text{Mn}_{0.25}\text{NiOOH}$ (Figure 4A). TEM confirms the existence of MnO_2 and metallic Mn (Figure 4B). Compared to $\text{Zn}_{0.25}\text{NiOOH}$, $\text{Zn}_{0.25}\text{@NiOOH}$ has peaks shifted towards lower wavenumber in the Raman spectra, which revealing a contraction of the crystalline lattice due to the Zn NPs exsolution (Figure 4C). Figure 4D further confirms the phenomenon of Zn exsolution. Moreover, a more comprehensive comparison by the DFT simulation also shows that various metal components are thermodynamically more favorable to *in situ* exsolve from the γ -NiOOH as compared to their counterparts from perovskites.^[20, 36-38] The segregation energy of *in situ* exsolving Cu and other transition metals (Mn, Fe, Co) from the γ -NiOOH framework (Figure 4E) is lower or on par with most exsolving atoms in perovskite frameworks. This suggests that similar exsolution approaches can be easily performed with a wide range of elements to form different NPs.

The results discussed herein showcase a new design principle for preparing stable metal nanoparticles for catalysis applications by *in situ* exsolution. This design principle may also be used to develop other alternative frameworks which can tackle the major challenges faced by conventional *in situ* exsolution technologies.

Catalysts based on supported metal nanoparticles (NPs) are broadly used in energy conversion and storage processes.^{1,2} The *in situ* exsolution with perovskites emerges as time-saving and cost-effective way to fabricate NPs catalysts,³⁻⁶ because of that this approach does not need multiple deposition steps or expensive precursors, while producing better-distributed and agglomeration-resistant metal NPs.⁷⁻¹⁰ However, the exsolution of NPs from perovskites (ABO_3) still faces several challenges. First of all, this process works with limited elements, as only the A/B sites with similar size can accommodate the formation of perovskite-type structure through a substitution mechanism. In addition, it is difficult to precisely control the composition of exsolved metal NPs due to the possibility of exsolution of both doping and doped metals.¹¹ Moreover, the exsolution approach poses high energy consumption as it is typically conducted at high temperatures of 700-1200 °C in a H_2 atmosphere.^{12,13} High temperature may also cause uncontrolled growth and coarsening of the NPs. Lastly, the growth of NPs takes a relatively long time (10–30 hours) due to sluggish kinetics.^{14,15} These drawbacks largely originate from the perovskite supporting framework. Therefore, in order to tackle these challenges, a new *in situ* exsolution supporting framework is needed.

Copper (Cu) has been well studied as the electrocatalysts for electrochemical reduction of CO_2 (ER CO_2).^{16,17} In particular, Cu NPs with smaller diameters (<6 nm) can prevent the hydrogenation of CO and favors the formation of synthetic gas (CO and H_2).¹⁸ However, the Cu NPs catalysts prepared in the wet-chemical impregnation or even traditional exsolution are generally not stable for longer operation due to susceptible agglomeration.¹⁹

Herein, we reported a new *in situ* exsolution of Cu NPs from nickel-based hydroxide (γ -NiOOH) with Cu cations confined in layer structures, denoted as Cu_xNiOOH , where x represents molar ratio of Cu to Ni (Figure 1A). *Ab initio* constrained molecular dynamics calculations demonstrate that the γ -NiOOH framework offers spontaneous *in situ* exsolution of Cu NPs from interstitial doped Cu, as evidenced by a negligible exsolution free energy barrier (~ 0.07 eV, Figure 1B). In comparison, a much higher free energy barrier of Cu exsolution from a typical $LaSrFeO_4$ perovskite²⁰ is found to be 4.54 eV, necessitating a high temperature for this process (Figure 1C). This result intrinsically underlines the advantage of exsolution of Cu_xNiOOH at mild condition, which is further corroborated by a comprehensive comparison with other perovskites in term of exsolution temperatures (Figure 1D).²⁰⁻²⁷

With the guidance of molecular simulation, we synthesized Cu_xNiOOH , then applied the electrical activation, the obtained samples are denoted as $Cu_x@NiOOH$ (Figure S1). The framework was proven to be predominantly γ -NiOOH with an intensive characteristic peak at 12.8° accompanied by tiny amount of β -Ni(OH) $_2$ and Ni(OH) $_2 \cdot 0.75H_2O$ in X-ray diffraction (XRD) patterns (Figure 2A). With the addition of copper, the peaks at 12.8° become sharpened and shift to lower angles, and no copper related peaks are observed when Cu/Ni ratio $\leq 1/2$, which is due to an expansion of γ -NiOOH crystalline lattice with the doping of coppers.²⁸ While at Cu/Ni ratio $\geq 1/2$, the peaks corresponding to $Cu(OH)_2 \cdot 2H_2O$ appear. This

suggests that the 1:2 Cu/Ni ratio is the upper limit of Cu doping, beyond which copper will exist as $\text{Cu}(\text{OH})_2$ outside of the $\gamma\text{-NiOOH}$ framework.

The doping process observed above is also supported by the X-ray photoelectron spectroscopy (XPS) results (Figure S2), which demonstrate the existence of Ni(II) and Ni(III) featured as the binding energies of the Ni $2p_{3/2}$ spectra fall at 855.3 to 856.5 eV for $\gamma\text{-NiOOH}$,^{29,30} whereas the Ni $2p_{3/2}$ spectra for Cu-doped $\gamma\text{-NiOOH}$ shift to a higher energy value caused by the interactions of copper-nickel d-d band.³¹ And the peak areas for the $\text{Cu}(\text{OH})_2$ species get higher with the increasing Cu doping level (Figure S3).

Moreover, Raman spectroscopy shows the existence of a wide peak located at $520\sim 550\text{ cm}^{-1}$ (Figure 2B). This is the E_g Ni-O bending vibration and A_{1g} Ni-O stretching vibration for $\gamma\text{-NiOOH}$.³² Compared to pristine $\gamma\text{-NiOOH}$, copper doped samples have peaks slightly shifted towards higher wavenumber, which can be attributed to lattice distortion caused by the doping of copper ions into the $\gamma\text{-NiOOH}$ structure.³³

X-ray absorption fine structure (XAFS) analysis shows that Cu was doped into the layered crystal structure of the $\gamma\text{-NiOOH}$ with an interstitial mechanism instead of the substitution mechanism observed with perovskites. Extended XAFS (EXAFS) fitting data reveals that the bond distances for Cu-O and Cu-Ni (Cu) are 1.95 Å and 3.14 Å (Figure S4, Table S1), respectively, which are larger than the distances for Ni-O (1.81 Å) and Ni-Ni (2.82 Å) in $\gamma\text{-NiOOH}$, ruling out the possibility of copper replacing Ni sites or embedding in any layer, instead copper is doped into the interstitial space of the $\gamma\text{-NiOOH}$ lattice. X-ray absorption near-edge structure (XANES) spectra further show that the doped Cu is in a +2 oxidation state as evidenced by the pre-edge intensity at 8970~8980 eV (Figure 2C). Further, no subnanometer Cu or CuO microcrystalline was observed because the absence of Cu-Cu scatterings (Figure S5).

The exsolution process of Cu from $\text{Cu}_{0.5}\text{NiOOH}$ results are monitored by TEM and Raman after the electrochemical activation. TEM shows dark dots are formed on the surface of $\text{Cu}_{0.5}\text{@NiOOH}$, which are not present on $\text{Cu}_{0.5}\text{NiOOH}$ (Figure 2D). These dots represent the interlayer spacings of 0.181, 0.198, 0.213, 0.203, and 0.273 nm, corresponding to the (1 1 0), (-1 1 1), and (1 1 1) planes of CuO, the (1 1 1) plane of Cu_2O , and the (2 0 0) plane of metallic Cu, respectively (Figure S6). We calculate the distribution of particle sizes based on Figure 2D, and the average size of exsolved Cu was ~4 nm (Figure S7A). Raman (Figure 2E) also confirms the existence of CuO (280, 321 cm^{-1}) and Cu_2O (623 cm^{-1}) in $\text{Cu}_{0.5}\text{@NiOOH}$, which are absence in $\text{Cu}_{0.5}\text{NiOOH}$.

To understand the exsolution at atomic level, we calculate the structure of $\gamma\text{-NiOOH}$ with one doped or exsolved Cu as shown in Figure 2F. Initially, the Cu cation is confined in NiOOH layers, coordinating with four O atoms, with an average bond length of 1.94 Å as that of the typical copper oxides.³⁴ With the cleavage of Cu-O mediated by electro-activation, Cu diffuses along the interlayers until stabilizing at the NiOOH (1 0 2) surface via a more weak Cu-O bonds with distance of ~ 2.10 Å. Figure 2G and Figure S8 further investigate the agglomeration with more Cu exsolved from bulk. It is interesting to find that less segregation energy is observed with the assembly of Cu, implying that a smaller size of copper would be

expected which are consistent with TEM results. A bader charge analysis determines the oxidation state of exsolved Cu close to zero with more Cu exsolved (Figure S9). Alternatively, under the working circumstances of negative potential (-0.3~-1.5 V vs. RHE), Cu cations are easy to be reduced to metallic state as reported by other literature.³⁵ It is noted that metallic Cu in Cu_x@NiOOH are easily oxidized when unavoidable exposure to air. Considering that Cu_{0.5}NiOOH are calcined in air but without copper oxides observed, the CuO and Cu₂O on Cu_{0.5}@NiOOH are likely formed by the oxidation of metallic Cu exsolved.

This new exsolution method offers several major advantages over the conventional perovskite-based framework (Figure 1D). Our exsolution can be achieved in as little as ~20 minutes through electrochemical activation at room temperature due to much lower barrier of 0.07 eV. In comparison, the exsolution with perovskites typically takes 10-30 hours due to the much higher energy of 4.54 eV. Moreover, our approach produces smaller Cu NPs (~4 nm) (Figure S7A) than a typical perovskite-based approach (10—2000 nm).²⁰⁻²⁷ As predicted by DFT results, the well-control of Cu NPs size is determined by segregation energy, which declines with more Cu exsolved, indicating that the formation of smaller Cu NPs is energy-favorable.

The exsolved Cu NPs from the γ -NiOOH exhibit high catalytic activity for ERCO₂ to CO (Table S2), which showing a volcano dependence on the size of exsolved Cu NPs resulting from different loading of doped Cu (Figure 3A, Figure S7B and S10), while the γ -NiOOH is also confirmed to be no activity, as no CO was observed (Figures 3C, S11 and S12), proving that exsolved Cu NPs are active sites.

Among all the tested catalysts, Cu_{0.5}@NiOOH with ~3.5 nm Cu NPs shows the highest activity for ERCO₂ (Figure 3A-3C), which can be explained by the availability of ultrafine Cu NPs exsolved from the framework. Specifically, at an applied potential of -0.7 V vs. RHE, the faradaic efficiency for CO (FE-CO) reached an unprecedented 95.6% with an acceptable CO current density (J_{CO}) of 10.6 mA cm⁻². In addition, The FE towards CO remains greater than 80% (Figure 3B) over a potential range between -0.5 V and -0.9 V.

To gain insight into the ERCO₂ performance of Cu_{0.5}@NiOOH, we investigated the electrochemical active surface area (ECSA). Larger ECSA indicates more active sites are available for the adsorption of reactants, thus facilitating CO evolution in ERCO₂. The ECSA of Cu_{0.5}@NiOOH (133.53 cm²) is 1.38, 1.22, 1.03, and 1.61 times larger than that of Cu₁@NiOOH (96.69 cm²), Cu_{0.7}@NiOOH (109.25 cm²), Cu_{0.3}@NiOOH (129.70 cm²), and NiOOH (82.86 cm²), respectively (Figure S13 and Table S3). These results further suggest that exsolved Cu NPs expose a large number of active sites. CO₂ adsorption measurements for Cu_{0.5}@NiOOH exhibited an excellent CO₂ adsorption capacity of 99.8 mg g⁻¹, which facilitates ERCO₂ (Figure S14).

Electrochemical impedance spectroscopy (EIS) analysis of Cu_{0.5}@NiOOH demonstrates the extremely low charge transfer resistance (R_{ct}) at the interface of the dip-coated catalyst and electrolyte (Figure 3D). Furthermore, the kinetics of the CO evolution was evaluated by tafel analysis. The tafel slop of

$\text{Cu}_{0.5}@\text{NiOOH}$ was measured to be 103 mV dec^{-1} (Figure 3E), suggesting fast kinetics for the CO formation, which is close to the theoretical value (118 mV dec^{-1}), indicating that the one electron transfer is the rate-determining step (RDS) for the generation of CO.

The exsolved Cu NPs demonstrate a notable electrochemical stability. Both the current density and the corresponding FE-CO are stable during a 40 h electrolysis process (Figure 3F). Additionally, TEM and Raman show that the microstructure of NiOOH and exsolved Cu NPs are maintained (Figure 2E and S15).

To demonstrate general applicability of *in situ* exsolution from metal doped γ -NiOOH, we further examined the case of Mn and Zn. Raman shows three bands centered at 467, 571 and 624 cm^{-1} in $\text{Mn}_{0.25}@\text{NiOOH}$ correspond to the MnO_2 , which are not present on $\text{Mn}_{0.25}\text{NiOOH}$ (Figure 4A). TEM confirms the existence of MnO_2 and metallic Mn (Figure 4B). Compared to $\text{Zn}_{0.25}\text{NiOOH}$, $\text{Zn}_{0.25}@\text{NiOOH}$ has peaks shifted towards lower wavenumber in the Raman spectra, which revealing a contraction of the crystalline lattice due to the Zn NPs exsolution (Figure 4C). Figure 4D further confirms the phenomenon of Zn exsolution. Moreover, a more comprehensive comparison by the DFT simulation also shows that various metal components are thermodynamically more favorable to *in situ* exsolve from the γ -NiOOH as compared to their counterparts from perovskites.^[20, 36-38] The segregation energy of *in situ* exsolving Cu and other transition metals (Mn, Fe, Co) from the γ -NiOOH framework (Figure 4E) is lower or on par with most exsolving atoms in perovskite frameworks. This suggests that similar exsolution approaches can be easily performed with a wide range of elements to form different NPs.

The results discussed herein showcase a new design principle for preparing stable metal nanoparticles for catalysis applications by *in situ* exsolution. This design principle may also be used to develop other alternative frameworks which can tackle the major challenges faced by conventional *in situ* exsolution technologies.

Declarations

Acknowledgments: We thank Dr. Siyu Yao for helpful comments on the XAFS data analysis. This work is supported by the National Natural Science Foundation of China (grant number 21676245), the National Key Research and Development Program of China (grant number 2018YFC0213806) and the Leading Innovative and Entrepreneur Team Introduction Program of Zhejiang (grant number 2019R01006).

Author contributions: M. C. W. and B. K. Z. performed the experiments. J. Q. D. performed the simulations. Y. H. designed the simulations and experiments. M. C. W, and P. F. X. analyzed the data. All authors discussed the results and wrote the manuscript.

Competing interests: Authors declare no competing interests.

Data and materials availability: All data is available in the main text or the supplementary materials.

References

1. Myung, J., Neagu, D., Miller, D. N. & Irvine, J. T. S. Switching on electrocatalytic activity in solid oxide cells. *Nature* **537**, 528-531 (2016).
2. Connor, P. A. *et al.* Tailoring SOFC Electrode Microstructures for Improved Performance. *Adv. Energy Mater.* **8**, 1800120 (2018).
3. Lu, J. *et al.* Coking- and Sintering-Resistant Palladium Catalysts Achieved Through Atomic Layer Deposition. *Science* **335**, 1205-1208 (2012).
4. Farmer, J. A. & Campbell, C. T. Ceria Maintains Smaller Metal Catalyst Particles by Strong Metal-Support Bonding. *Science* **329**, 933-936 (2010).
5. Kim, S. *et al.* Nanostructured Double Perovskite Cathode With Low Sintering Temperature For Intermediate Temperature Solid Oxide Fuel Cells. *ChemSusChem* **8**, 3153-3158 (2015).
6. Szuromi, P. Watching metal nanoparticle exsolution. *Science* **366**, 834.4-835 (2019).
7. Zhu, T. *et al.* Exsolution and electrochemistry in perovskite solid oxide fuel cell anodes: Role of stoichiometry in Sr(Ti,Fe,Ni)O₃. *J. Power Sources* **439**, 227077 (2019).
8. Nishihata, Y. *et al.* Self-regeneration of a Pd-perovskite catalyst for automotive emissions control. *Nature* **418**, 164-167 (2002).
9. Cali, E. *et al.* Exsolution of Catalytically Active Iridium Nanoparticles from Strontium Titanate. *ACS Appl. Mater. Interfaces* **12**, 37444-37453 (2020).
10. Neagu, D. *et al.* Demonstration of chemistry at a point through restructuring and catalytic activation at anchored nanoparticles. *Nat. Commun.* **8**, 1855 (2017).
11. Zhang, J., Gao, M.-R. & Luo, J.-L. In Situ Exsolved Metal Nanoparticles: A Smart Approach for Optimization of Catalysts. *Chem. Mater.* **32**, 5424-5441 (2020).
12. Sun, Y. F. *et al.* New Opportunity for in Situ Exsolution of Metallic Nanoparticles on Perovskite Parent. *Nano Lett.* **16**, 5303-5309 (2016).
13. Neagu, D. *et al.* In Situ Observation of Nanoparticle Exsolution from Perovskite Oxides: From Atomic Scale Mechanistic Insight to Nanostructure Tailoring. *ACS Nano* **13**, 12996-13005 (2019).
14. Neagu, D., Tsekouras, G., Miller, D. N., Ménard, H. & Irvine, J. T. S. In situ growth of nanoparticles through control of non-stoichiometry. *Nat. Chem.* **5**, 916-923 (2013).
15. Neagu, D. *et al.* Nano-socketed nickel particles with enhanced coking resistance grown in situ by redox exsolution. *Nat. Commun.* **6**, 8120 (2015).

16. Dai, L. *et al.* Ultrastable atomic copper nanosheets for selective electrochemical reduction of carbon dioxide. *Sci. Adv.* **3**, e1701069 (2017).
17. Mun, Y. *et al.* Cu-Pd alloy nanoparticles as highly selective catalysts for efficient electrochemical reduction of CO₂ to CO. *Appl. Catal. B Environ.* **246**, 82-88 (2019).
18. Reske, R., Mistry, H., Behafarid, F., Roldan Cuenya, B. & Strasser, P. Particle Size Effects in the Catalytic Electroreduction of CO₂ on Cu Nanoparticles. *J. Am. Chem. Soc.* **136**, 6978-6986 (2014).
19. Manthiram, K., Beberwyck, B. J. & Alivisatos, A. P. Enhanced electrochemical methanation of carbon dioxide with a dispersible nanoscale copper catalyst. *J. Am. Chem. Soc.* **136**, 13319-13325 (2014).
20. Fu, L. *et al.* Exsolution of Cu nanoparticles in (LaSr)_{0.9}Fe_{0.9}Cu_{0.1}O₄ Ruddlesden-Popper oxide as symmetrical electrode for solid oxide cells. *Appl. Surf. Sci.* **511**, 145525 (2020).
21. Adjianto, L., Balaji Padmanabhan, V., Küngas, R., Gorte, R. J. & Vohs, J. M. Transition metal-doped rare earth vanadates: A regenerable catalytic material for SOFC anodes. *J. Mater. Chem.* **22**, 11396-11402 (2012).
22. Lu, J. *et al.* Highly efficient electrochemical reforming of CH₄/CO₂ in a solid oxide electrolyser. *Sci. Adv.* **4**, (2018).
23. Wang, W., Zhu, C., Xie, K. & Gan, L. High performance, coking-resistant and sulfur-tolerant anode for solid oxide fuel cell. *J. Power Sources* **406**, 1-6 (2018).
24. Xu, Z. *et al.* A High Performance Ni-Free Redox Reversible Ceramic Anode R-La_{0.5} Sr_{0.5} Fe_{0.8} Cu_{0.1} Ti_{0.1} O_{3-δ} for Intermediate Temperature Solid Oxide Fuel Cells. *J. Electrochem. Soc.* **163**, F737-F743 (2016).
25. Lu, J., Yin, Y. M., Li, J., Xu, L. & Ma, Z. F. A cobalt-free electrode material La_{0.5}Sr_{0.5}Fe_{0.8}Cu_{0.2}O_{3-δ} for symmetrical solid oxide fuel cells. *Electrochem. commun.* **61**, 18-22 (2015).
26. Li, H. *et al.* Chromate cathode decorated with in-situ growth of copper nanocatalyst for high temperature carbon dioxide electrolysis. *Int. J. Hydrogen Energy* **39**, 20888-20897 (2014).
27. Qi, W. *et al.* Reversibly in-situ anchoring copper nanocatalyst in perovskite titanate cathode for direct high-temperature steam electrolysis. *Int. J. Hydrogen Energy* **39**, 5485-5496 (2014).
28. Huang, G. *et al.* Postsynthetic Doping of MnCl₂ Molecules into Preformed CsPbBr₃ Perovskite Nanocrystals via a Halide Exchange-Driven Cation Exchange. *Adv. Mater.* **29**, 1700095 (2017).
29. Naghash, A. R., Etsell, T. H. & Xu, S. XRD and XPS Study of Cu-Ni Interactions on Reduced Copper-Nickel-Aluminum Oxide Solid Solution Catalysts. *Chem. Mater.* **18**, 2480-2488 (2006).

30. Liang, J. *et al.* Self-supported nickel nitride nanosheets as highly efficient electrocatalysts for hydrogen evolution. *Appl. Surf. Sci.* **503**, 144143 (2020).
31. Bai, D. *et al.* Interstitial Mn²⁺-Driven High-Aspect-Ratio Grain Growth for Low-Trap-Density Microcrystalline Films for Record Efficiency CsPbI₂Br Solar Cells. *ACS Energy Lett.* **3**, 970-978 (2018).
32. Huang, J. *et al.* Identification of Key Reversible Intermediates in Self-Reconstructed Nickel-Based Hybrid Electrocatalysts for Oxygen Evolution. *Angew. Chemie Int. Ed.* **58**, 17458-17464 (2019).
33. Niishiro, R., Tanaka, S. & Kudo, A. Hydrothermal-synthesized SrTiO₃ photocatalyst codoped with rhodium and antimony with visible-light response for sacrificial H₂ and O₂ evolution and application to overall water splitting. *Appl. Catal. B Environ.* **150-151**, 187-196 (2014).
34. Soon, A., Todorova, M., Delley, B. & Stampfl, C. Thermodynamic stability and structure of copper oxide surfaces: A first-principles investigation. *Phys. Rev. B - Condens. Matter Mater. Phys.* **75**, 125420 (2007).
35. Chen, C. *et al.* Cu-Ag Tandem Catalysts for High-Rate CO₂ Electrolysis toward Multicarbon. *Joule* **4**, 1688-1699 (2020).
36. Lv, H. *et al.* In Situ Investigation of Reversible Exsolution/Dissolution of CoFe Alloy Nanoparticles in a Co-Doped Sr₂Fe_{1.5}Mo_{0.5}O_{6-δ} Cathode for CO₂ Electrolysis. *Adv. Mater.* **32**, e1906193 (2020).
37. Ding, S. *et al.* A-site deficient perovskite with nano-socketed Ni-Fe alloy particles as highly active and durable catalyst for high-temperature CO₂ electrolysis. *Electrochim. Acta* **335**, 135683 (2020).
38. Kwon, O. *et al.* Exsolution trends and co-segregation aspects of self-grown catalyst nanoparticles in perovskites. *Nat. Commun.* **8**, 15967 (2017).

Figures

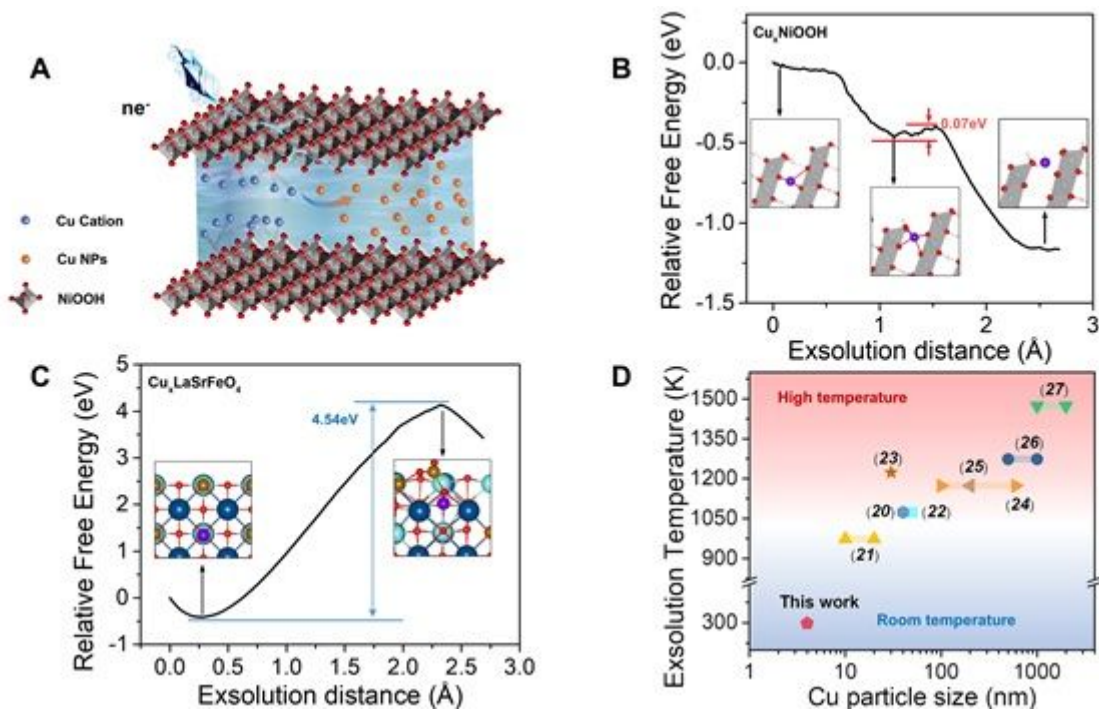


Figure 1

(A) Schematic diagram of exsolving metal nanoparticles from the interstitial spaces of γ -NiOOH. The relative free energy of Cu atoms along the exsolution processes for (B) γ -NiOOH and (C) LaSrFeO₄ perovskite. (D) Exsolution temperature and exsolved Cu particle size of various comparative catalysts. The purple, cyan, blue, brown, and red spheres represent Cu, Sr, La, Fe, and O atoms, respectively.

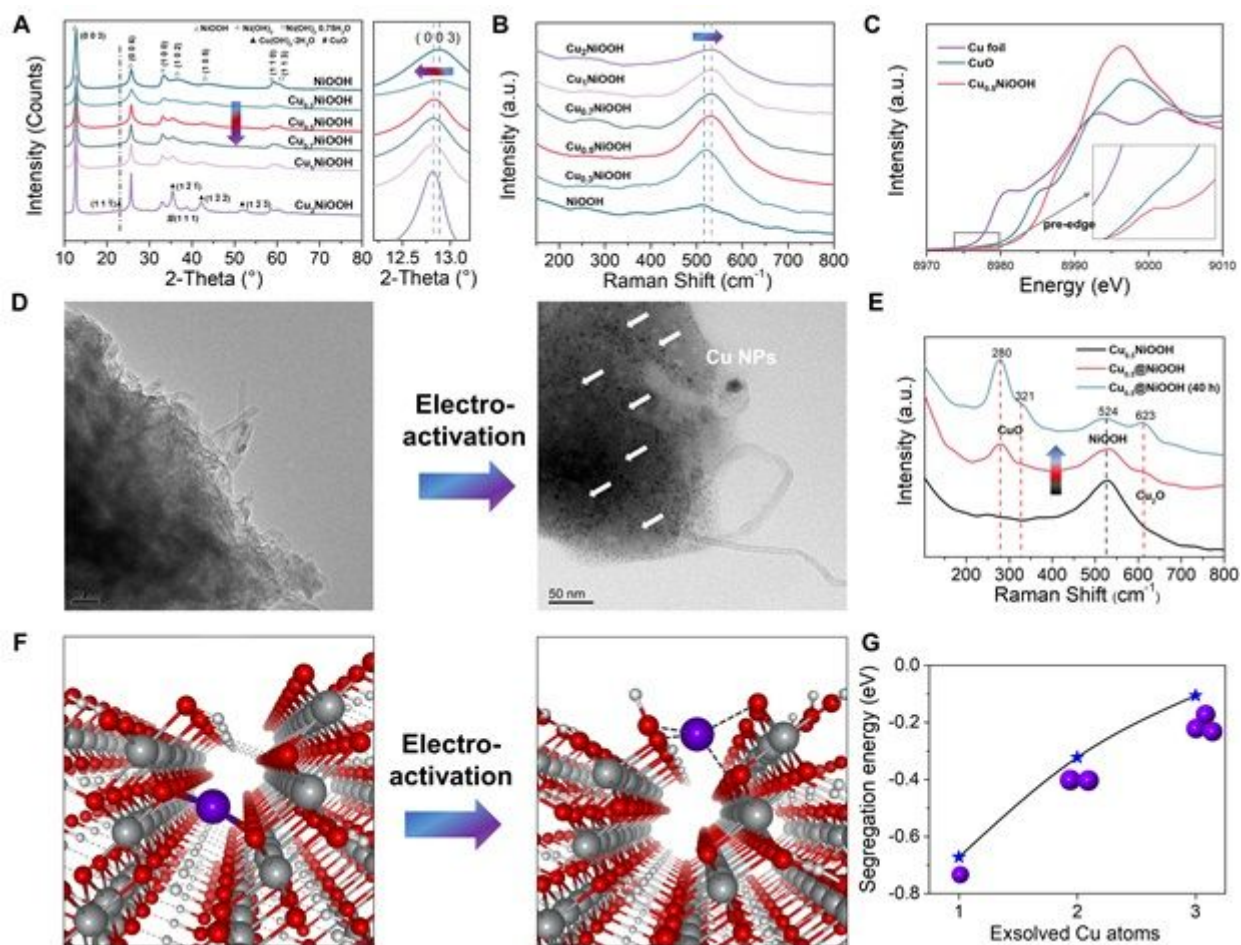


Figure 2

(A) XRD patterns and (B) UV Raman spectroscopy of the Cu_xNiOOH catalysts. (C) Cu K-edge X-ray absorption near-edge structure (XANES) spectra of Cu foil, CuO, and Cu_{0.5}NiOOH catalysts. (D) TEM micrograph of Cu_{0.5}NiOOH and Cu_{0.5}@NiOOH catalysts. (E) Raman patterns for Cu_{0.5}NiOOH, Cu_{0.5}@NiOOH and Cu_{0.5}@NiOOH (used for 40 h). (F) Simulation models for Cu exsolution. (G) Segregation energy of exsolving more Cu atoms.

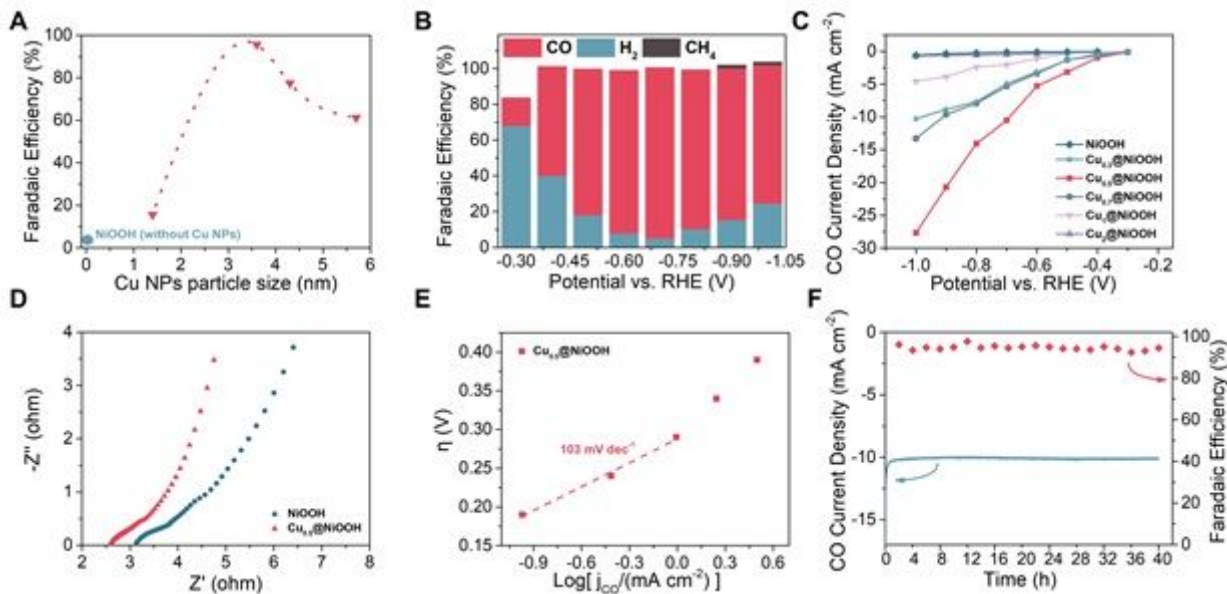


Figure 3

(A) Faraday efficiency with Cu NPs particle size. (B) Faradaic efficiency towards CO, H₂, and CH₄ at different potentials for Cu_{0.5}@NiOOH. (C) CO current density at different potentials for NiOOH and exsolved-catalysts. (D) EIS nyquist analysis of NiOOH and Cu_{0.5}@NiOOH. (E) Tafel plot and (F) Long-term stability testing of Cu_{0.5}@NiOOH electrode over 40 h.

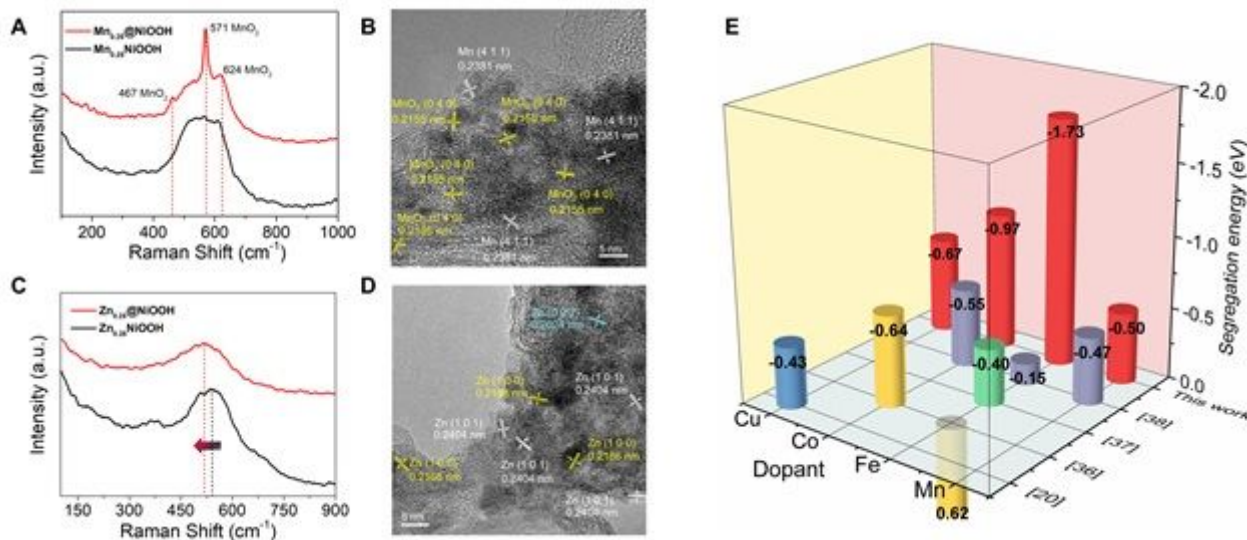


Figure 4

(A) Raman spectroscopy for Mn_{0.25}NiOOH and Mn_{0.25}@NiOOH. (B) TEM for Mn_{0.25}@NiOOH. (C) Raman spectroscopy for Zn_{0.25}NiOOH and Zn_{0.25}@NiOOH. (D) TEM for Zn_{0.25}@NiOOH. (E) Segregation energies of transition metal dopants in different hosts.

Supplementary Files

This is a list of supplementary files associated with this preprint. Click to download.

- [Supportinginformation.docx](#)